https://doi.org/10.5194/gmd-2020-150
Preprint. Discussion started: 7 July 2020

Geoscientific Model Development Discussions

Configuration and Evaluation of a Global Unstructured Mesh Model based on the Variable-Resolution Approach

Yihui Zhou[1,2], Yi Zhang[3], Jian Li[3], Rucong Yu[3], Zhuang Liu[4]

[1]State Key Laboratory of Numerical Modeling for Atmospheric Sciences and Geophysical Fluid Dynamics (LASG), Institute of Atmospheric Physics, Chinese Academy of Sciences, Beijing, China
[2]University of Chinese Academy of Sciences, Beijing, China
[3]State Key Laboratory of Severe Weather (LaSW), Chinese Academy of Meteorological Sciences, China Meteorological Administration, Beijing, China
[4]National Supercomputing Center in Wuxi, Jiangsu, China

Correspondence to: Yi Zhang (yizhang@cma.cn)

Abstract. Targeting a long-term effort towards a global weather and climate model with a local refinement function, this study systematically configures and evaluates the performance of an unstructured model based on the variable-resolution (VR) approach. Aided by the idealized dry- and moist-atmosphere tests, the model performance is examined in an intermediate degree of complexity. The dry baroclinic wave simulations suggest that the 3D VR-model can reproduce comparable solutions in the refined regions as a fine-resolution quasi-uniform (QU) mesh model, although the global errors increase. The variation of the mesh resolution in the transition zone does not adversely affect the wave pattern. In the coarse-resolution area, the VR model simulates a similar wave distribution to the low-resolution QU model. Two multi-region refinement approaches, including the hierarchical and polycentric refinement modes, further testify the model performance under a more challenging environment. The moist idealized tropical cyclone test further enables us to examine the model ability in terms of resolving fine-scale structures. It is found that the VR model can have the tropical cyclone stably pass the transition zone in various configurations. A series of sensitivity tests examines the model performance in a hierarchical refinement mode, and the solutions exhibit consistency even when the VR mesh is slightly perturbed by one of the three parameters that control the density function. Moreover, only the finest resolution has a dominant impact on the fine-scale structures in the refined region. The tropical cyclone, starting from the 2nd-refinement region and passing through the inner transition zone, gets intensified and possesses a smaller area coverage in the refined regions, as compared to the QU-mesh model that has the same number of grid points. Such variations are consistent with the behavior that one may observe when uniformly refining the QU-mesh model. Besides the horizontal resolution, the intensity of the tropical cyclone is also influenced by the Smagorinsky horizontal diffusion coefficient. The VR model exhibits higher sensitivity in this regard, suggesting the importance of parameter tuning and proper model configurations.

1 Introduction

Increasing resolution is generally regarded as an effective way to improve global weather and climate modeling (e.g., Jung et al., 2012; Wehner et al., 2014; Zhang et al., 2014; Yu et al., 2019). As the model resolution continuously increases, much more computational resources are required, constituting a major challenge for efficient model development and applications. This has led to the pursuit of locally refined, variable-resolution (VR) modeling approaches. Unlike nested regional modeling with prescribed lateral boundaries, the VR approach maintains the global modeling configuration while permits increased resolution for certain regions of interest. Numerical modeling experience has shown that such an approach can preserve the benefits of high-resolution modeling for the region of interest at a lower computational cost, as the total number of the grid points can be largely reduced (e.g., Sabin et al.,

https://doi.org/10.5194/gmd-2020-150
Preprint. Discussion started: 7 July 2020

2013; Rauscher and Ringler, 2014; Sakaguchi et al., 2015; Gettelman et al., 2018).

Although the VR models can achieve improvements in the region of interest, they may potentially suffer from some problems. The nonuniform mesh degrades the global accuracy (St-Cyr et al., 2008; Weller et al., 2009). Thus, it is important to maximize the model performance for the refined region, while retains or minimally degrades the performance for other non-refined regions. Previous studies have investigated the impacts of local grid refinements on the solution error for global atmospheric models (e.g., Ringler et al., 2008; Park et al., 2013), mainly based on the single-region refinement. A suite of 2D shallow-water VR-model tests demonstrates that the solution error is primarily controlled by the coarsest region (Ringler et al., 2011). Model sensitivities to the width of the grid transition zone and the densifying ratio are primary foci, and have been examined by utilizing various test cases. Based on the spherical centroid Voronoi tessellation (SCVT), Ringler et al., (2011) suspected that the width of the transition zone may lead to increased errors. Liu and Yang (2017) suggested that the width of the transition zone may cause less additional errors as compared to the increase of the densifying ratio. Rapid resolution variations may also lead to wave distortion and artificial wave reflection in the transition zone. Within a unified global model framework, these problems in the transition zone and the low-resolution region may potentially deteriorate the performance in the refined region. Given the cost of accuracy, a primary question arises, that is, whether a VR model can generate a comparable simulation in the refined region compared to the high-resolution quasi-uniform (QU) model, especially in a more diverse VR environment.

A primary motivation of increasing resolution is to resolve fine-scale atmospheric fluid structures. Tropical cyclone is a useful testbed and has been frequently used to examine resolution sensitivity. High-resolution global models show their improvement in tropical cyclone statistics as the resolution increases (e.g., Walsh et al., 2012; Strachan et al., 2013; Bacmeister et al., 2014). The global VR approach has also been explored to simulate tropical cyclones for cost-effective climate simulations (e.g., Zarzycki and Jablonowski, 2014). Unlike the adverse influence caused by the boundary forcing in a nested regional model, the VR model captures smoother cloud patterns and smoother mid-level jet structures, producing enhanced tropical cyclone activities (Hashimoto et al., 2015). Based on the VR meshes, the Community Atmosphere Model well maintains the tropical cyclone crossing the transition zone without discernable wave reflection or grid imprinting (Zarzycki et al., 2014). The simulations of such synoptic-scale system crossing the transition zone are of vital importance to the model stability, especially under higher resolution conditions.

While previous studies (e.g., Rauscher et al., 2013; Harris et al., 2016; Huang et al., 2016) have reported benefits of VR modeling, how to properly utilize this technique is still a challenging task and deserves ongoing exploration (e.g., Guba et al., 2014; Düben and Korn, 2014; Hendricks et al., 2016). In this study, we systematically configure and evaluate the Global-to-Regional Integrated forecast SysTem (GRIST) Atmosphere framework based on the VR approach. GRIST is a global model built on an unstructured Voronoi-Delaunay mesh. In previous studies, the component performance in shallow water environment (Zhang, 2018; Wang et al., 2019), 3D dry dynamics (Zhang et al., 2019) and idealized moist-atmosphere environment (Zhang et al., 2020) have been assessed in detail, mainly based on the QU-mesh simulations. Neither the dry dynamical core (dycore hereafter) nor the dycore-tracer-physics (DTP hereafter) split-coupling mechanism were systematically exposed to the more challenging VR configuration. It remains unknown whether the model is able to behave properly when the local mesh variation is considered. The idealized test cases drive the model towards some well-expected behaviors, facilitating some basic understanding of VR modeling. The major objects of this study are:

(i) To validate the behavior of the dynamical model in its VR configuration, and to understand the strength and weakness under various refinement meshes;

(ii) To provide a general guidance of utilizing different-style VR refinements for more realistic modeling in future.

To achieve these goals, we first evaluate the VR model performance in dry baroclinic wave test cases based on

https://doi.org/10.5194/gmd-2020-150
Preprint. Discussion started: 7 July 2020

Geoscientific Model Development Discussions

three different initial point sets. We focus on the ability of the VR model to match the QU-mesh solutions in the refined regions, and the model stability in terms of waves crossing through the transition zones. To balance the accuracy and computational cost, we test the model in two multi-region refinement modes, which are more flexible for enlarging the effective coverage of the fine-resolution regions given a certain number of grid points. The performance under the moist-physics configuration is examined by using an idealized tropical cyclone test. A series of numerical tests was performed to examine the model reliability under more challenging conditions.

The remainder of this paper is organized as follows. Section 2 describes the model and mesh generation. Section 3 examines the performance of the VR model against the QU one based on dry-atmosphere simulations. The model performance under higher-resolution conditions with various mesh refinement modes is also investigated. Section 4 documents model sensitivity based on moist-atmosphere simulations. Section 5 presents a summary.

2 Model and mesh generation

2.1 Model and configurations

The model evaluated here is a developing version of the Global-to-Regional Integrated forecast SysTem (GRIST) Atmosphere framework, the version is named after the last two numbers of the solar calendar year (i.e., GRIST-A20). The code is able to exactly regress to the state reported in Zhang et al. (2020), although significant code refactoring is continuously added. It uses an unstructured-mesh formulation, which permits the use of SCVT (Ringler et al., 2008; Jacobsen et al., 2013) that enables VR modeling. The dycore framework is described and evaluated in Zhang et al. (2019). The moist atmospheric model is equipped with a general physics-dynamics coupling workflow that has a DTP split-coupling mechanism, and details were described in Zhang et al., 2020. The dry-mass coordinate allows a switch between the hydrostatic and nonhydrostatic solvers, and exactly (to machine roundoff) conserves the dry air mass. The 3D tracer transport module has several horizontal and vertical options for various applications (cf., Zhang et al., 2020). In this study, the Two-step Shape-Preserving Advection Scheme (TSPAS; Zhang et al., 2017; Yu, 1994) was used as the horizontal one, and a Runge-Kutta based third-order upwind scheme (Wicker and Skamarock, 2002) is used as the vertical one.

In this study, we employ both the nonhydrostatic and hydrostatic dynamical core. Results of the high-resolution QU-mesh model are used as a reference for evaluating the performance of the VR model. We use a physically-based Smagorinsky horizontal diffusion (Smagorinsky, 1963) with the second-order Laplacian operators. It is activated in all dry and moist experiments except for the dry test on the lowest-resolution QU mesh (i.e., G6 in this study). For the moist simulations, we couple the model with a simple-physics package that has important driving mechanisms for tropical cyclones (Reed and Jablonowski, 2012), which provides a higher degree of complexity than the dry simulations. A summary of the mesh resolution and timesteps for each experiment is given in the supplement file (Table S1, S2).

2.2 Generation of the variable-resolution mesh

Technically, running an unstructured-mesh model in a VR configuration only requires altering the mesh file (when idealized test cases are considered). A detailed description of the properties and generation of the SCVT is provided in Ringler et al. (2011) and Ju et al. (2011). In this study, we focus on two key elements of the SCVT: generators and density function. A spherical Voronoi tessellation is a spatial subdivision of a sphere Ω based on a set of distinct points on Ω. For each point x_i, $i = 1, \dots, n$, the corresponding Voronoi region V_i, $i = 1, \dots, n$, is defined by:

$$V_i = \{x \in \Omega \mid \|x - x_i\| < \|x - x_j\| \;\; for\; j = 1, \dots, n\; and\; j \neq i\}, \qquad (1)$$

where $\|\cdot\|$ denotes the geodesic distance. Each point x_i is called a generator and its corresponding Voronoi region V_i

https://doi.org/10.5194/gmd-2020-150
Preprint. Discussion started: 7 July 2020

Geoscientific Model Development Discussions

is also called the Voronoi cell. A spherical Voronoi tessellation mesh becomes a SCVT mesh when the generators are also the centroids of the corresponding Voronoi regions, which are derived from a density function defined on Ω. In this study, the SCVT mesh is constructed via an iterative process based on the Lloyd's algorithm (Du et al., 1999). In our implementation, the iteration continues until the circumcenter of each Delaunay triangle falls within the triangle. Instead of the time-consuming serial construction, we generate the VR tessellation based on a parallel algorithm (Jacobsen et al., 2013).

2.2.1 Generators

In this study, we use three different ways to construct the original generators.

(i) **Icosahedron bisection**. The icosahedron-based SCVT meshes benefit the excellent uniform properties due to bisections of a regular icosahedron. We use the vertexes of the polyhedron after icosahedral bisections as the initial generators for constructing the SCVT. The mesh resolution is referred to as Grid-level/Gn, where n denotes the number of bisections. After each bisection, the grid points of the meshes are approximately four times more than the former one.

(ii) **Icosahedron bisection with a final-step trisection**. Given the requirement for less computational cost, less generators are desired to be used for the VR mesh than the uniform high-resolution mesh. If the VR mesh (one based on refining the QU mesh) uses the same number of points as the one-level-lower QU mesh, the densifying ratio between the fine- and coarse-resolution regions has to be quite large to achieve fine enough resolution in the refined region. Too large densifying ratio may lead to much larger simulation errors. Here, we conduct a final-step trisection (B3) instead of the bisection to achieve an intermediate resolution between two neighboring G-level resolutions. For instance, the resolution of the QU G5B3 mesh (~80 km) is three times finer than G5 (~240 km), between G6 (~120 km) and G7 (~60 km). The number of the added primal cells (mainly hexagons) from G5 to G5B3 is equal to four times the number of the dual cells (triangles) in G5.

(iii) **Spherical uniform random (SUR) set of points**. Initial points are created uniformly on the sphere Ω by the Monte Carlo method (Metropolis and Ulam, 1949). In this way, the set of generators can be obtained by using an arbitrary number of initial points, not restricted to the fixed number of points as in the icosahedron bisection.

2.2.2 Density function

The advantage of the SCVT is their freedom to specify the density function. For any two Voronoi regions indexed by i and j, the conjecture is:

$$\frac{dx_i}{dx_j} \approx \left[\frac{\rho(x_j)}{\rho(x_i)}\right]^{1/4}, \qquad (2)$$

where $\rho(x_i)$ is the density function evaluated at x_i, and dx_i measures the local mesh resolution (Ju, 2007). By specifying the density function, the SCVT meshes are able to precisely control the distribution of the local resolution, which provides a convenient way for various refinement modes.

A QU mesh forms when the density is constant on the sphere, and the Voronoi region is approximately equivalent to each other. The basic density function for the VR SCVT in this study is expressed as:

$$\rho(x_i) = \frac{1}{2(1-\gamma)}\left[\tanh\left(\frac{\beta - \|x_{rc} - x_i\|}{\alpha}\right) + 1\right] + \gamma, \qquad (3)$$

where $\|x_{rc} - x_i\|$ denotes the geodesic distance between the location of the refinement center and each generator lying on the surface of the sphere. Here, α indicates the width of the transition zone between the fine-resolution and coarse-resolution regions; β defines the coverage radius of the fine-resolution region; γ measures the densifying ratio of the

https://doi.org/10.5194/gmd-2020-150
Preprint. Discussion started: 7 July 2020

Geoscientific Model Development Discussions
Open Access

mesh resolution between the fine and coarse regions. The densifying ratio should better have an moderate value, e.g., no greater than 1:4 (Liu and Yang, 2017), to constrain the solution error. To balance the demand for less grid points and smaller errors, we fix $\gamma = (1/4)^4$ in this study, marked as X4.

The basic density function is flexible to adjust the mesh because of its three-parameter space, but it can only be used for a single-region refinement. Here, we adjust the basic density function for multi-region refinement. The multi-region refinement is divided into two different modes based on the refinement centers. In a hierarchical refinement mode, we add a uniform intermediate-resolution region between the inner fine-resolution and the outer coarse-resolution regions. Eq. (3) can be generalized to a form that allows to control the resolution of the intermediate region:

$$\rho(x_i) = \frac{1}{2(1-\gamma)}\left[\frac{1-\lambda}{1-\gamma}\tanh\left(\frac{\beta_1-\|x_{rc}-x_i\|}{\alpha_1}\right) + \frac{\lambda-\gamma}{1-\gamma}\tanh\left(\frac{\beta_2-\|x_{rc}-x_i\|}{\alpha_2}\right) + 1\right] + \gamma. \quad (4)$$

λ is designed to control the resolution of the intermediate-resolution region, also referred to as the 2nd-refinement region (dx_{r_2}) that is located between the 1st-refinement (dx_{r_1}) and the coarse-resolution regions (dx_c):

$$\frac{dx_{r_1}}{dx_{r_2}} \approx \lambda^{1/4}. \quad (5)$$

The function of γ is similar to that in the previous single-region refinement, except that the fine-resolution region is referred to as the 1st-refinement region here:

$$\frac{dx_{r_1}}{dx_c} \approx \gamma^{1/4}. \quad (6)$$

Corresponding to γ, we refer to the meshes that are generated based on λ values of $(1)^4$, $(1/2)^4$, and $(1/3)^4$ as XL1, XL2, and XL3 meshes, since the resolutions of the 1st-refinement and the 2nd-refinement region vary according to the inner densifying ratios of 1, 2, and 3, respectively. Generally, the value of λ is between γ and 1. Under such circumstances, a hierarchical densifying mode mesh will be finally constructed via the iterative procedure (Fig. 1). As γ is fixed at X4, the hierarchical meshes in this study are called X4L1, X4L2, and X4L3 meshes for short. In a polycentric refinement mode, by adding a different refinement center x_{rc2}, the density function of the polycentric refinement mode is defined as:

$$\rho(x_i) = \frac{1}{2(1-\gamma)}\left[\tanh\left(\frac{\beta-\|x_{rc1}-x_i\|}{\alpha}\right) + \tanh\left(\frac{\beta-\|x_{rc2}-x_i\|}{\alpha}\right) + 2\right] + \gamma. \quad (7)$$

The geodesic distance between the two refinement centers must satisfy $\|x_{rc1} - x_{rc2}\| > 2\beta$.

3 Dry-atmosphere simulations

3.1 Single-region refinement

The dry-atmosphere test examines the pure numerical solution of the model. It does not include the nonlinear interaction between dynamics, moisture transport and parameterization. To evaluate the performance of the VR model, we first compare the model dynamics with that simulated by a QU configuration, based on the dry baroclinic wave test case of Jablonowski and Williamson (2006). The QU meshes used here include G6 (~120 km; 40,962 cells), G7 (~60 km; 163,842 cells), and G8 (~30 km; 655,362 cells). Three types of generators for constructing the VR meshes are obtained based on: (i) icosahedral bisection (G6X4), (ii) final-step trisection (G5B3X4), and (iii) spherical uniform random points (SURX4). The minimum iteration number is 300,000 for G6X4, and 1,000,000 for both G5B3X4 and SURX4. To assess the simulated baroclinic waves in the refined and transition regions, x_{rc} is located at [180° E, 35° N], with $\alpha = \pi/20$ and $\beta = \pi/6$. Figure 2 displays an example of the X4 meshes used for this test.

Figure 3 shows the global distribution of surface pressure at day 9 simulated by the nonhydrostatic core in the baroclinic wave test. The location and magnitude of the high- and low-value centers in the three VR simulations (Figs. 3d-3f) well match those in the QU-mesh solutions (Figs. 3a-3c). Due to the asymptotic density function used for the VR meshes, we find some grid imprinting patterns in G6X4. In the G5B3X4 case, the distribution of surface pressure in the equatorial region well coincides with that of G8. The grid imprinting pattern in the southern hemisphere still exists, but has been slightly alleviated as compared to G6X4. The distribution of surface pressure in SURX4 is similar to G8 except for the grid imprinting pattern in the coarse region.

To quantify the influence of the VR meshes on the solution accuracy, we calculated the global level 2 (l_2) error norms for surface pressure. The error in each simulation is computed against the G8 solution. The evolution of the l_2 error in the hydrostatic solver (Fig. 4a) is close to that in the nonhydrostatic one (Fig. 4b). During the first 10 days, the l_2 errors in all VR simulations are close to that of G6. Among the three VR meshes, the l_2 value of the G6X4 test is the largest, but its error in the nonhydrostatic test is slightly smaller than that in the hydrostatic test. In the nonhydrostatic model, the curve of G6X4 almost lies within the uncertainty regime that represents the maximum error norm within the hydrostatic and nonhydrostatic models. In general, the solution accuracy of two solvers is comparable.

As for the QU meshes, the l_2 error in the G7 test is overall smaller than G6. An increase in the number of generators greatly eliminates the grid imprinting in the globe. As for the VR meshes, the difference in l_2 errors between SURX4 and G5B3X4 reflects the influence of the distribution of the initial generators on the mesh quality. The SURX4 model possesses more grid points, but its solution error is slightly higher than G5B3X4 at all 15 days. This implies that the randomly generated initial points are more likely to be trapped into the local area during the iterative procedure of mesh generation, leading to more local mesh irregularities. Owing to the more well-distributed initial points, the error in the G5B3X4 simulation is mostly smaller than that in the QU G6 during the first 10 days.

Figure 5 illustrates the distribution of relative vorticity at the model level near 850 hPa after 10 simulation days. Note that these values are displayed on the original unstructured triangular cell that defines vorticity, so the oscillation at the smallest grid space (more conspicuous for the coarse resolution; e.g., Fig. 5a) reflects the grid shape rather than grid-scale noise (see the QU results interpolated to the regular longitude-latitude grids in Fig. S1). As the resolution increases, the QU model produces stronger vortices with an evident filament structure (Figs. 5a-5c). In the VR model, the two vortices in the west fall within the fine-resolution regions. The structure of the westernmost vortex in the G6X4 simulation (Fig. 5d) is close to G8. The G5B3X4 test (Fig. 5e) captures the fine-scale structure of the two vorticity centers. The magnitudes of the westernmost vortex in G5B3X4 are even closer to those in G8 than G7. When more points are used, as shown in SURX4 (Fig. 5f), both the simulated structure and the magnitudes of vorticities are further improved. The easternmost vortex falls within the transition zone across the fine and coarse resolution. The variation of the mesh sizes there has little impact on the shape of the vortex. The structure and intensity of the vortex are better simulated by G5B3X4 as compared to G6X4. Although the mesh resolutions in the transition zone are coarser than the fine-resolution regions, the pattern of the vortices in G5B3X4 and SURX4 is quite close to that in G8.

The VR model generally simulates the smooth structure of the vortices in the refined region, as the high-resolution QU model. In the SURX4 test, however, a slight roughness is found on the tails of the vortices. This defect is largely caused by local mesh irregularities. Compared to the icosahedron-based SCVT meshes, the random initial generators degrade the mesh quality and the simulation performance. Nevertheless, the deterioration hardly does harm to the pattern and magnitude of the vorticity. Corresponding to grid imprinting in the surface pressure over the southern hemisphere, the relative vorticity distributions there in the VR simulations are not as uniform as that in the QU models (figure not shown).

To have a more quantitative evaluation of the momentum field, the horizontal kinetic energy spectra are investigated. The QU-mesh simulation data have been interpolated to T106 (G6), T213 (G7), and T426 (G8) Gaussian grids for spherical harmonic analysis. The VR data have been interpolated to T106. The total kinetic energy spectra of the nonhydrostatic and hydrostatic cores are quite close to each other (Figs. 6a, 6d). For the high wave numbers, the curves of G5B3X4 and SURX4 are close to G8. This proves that the VR model is able to resolve fine-scale structure in its refined region. Near the wave number of 100, the curve of G5B3X4 coincides well with G8 regarding both the rotational and divergence component. At such high wave numbers, SURX4 is even closer to G8 in the rotational component due to the increased number of grid points. Regarding the divergence component, SURX4 suffers from the tiny fluctuations due to local irregular grids at high wave numbers. However, the entire curve of SURX4 overall matches that of G8.

Previous VR modeling based on the shallow water tests has found that the error in the refined region can be significantly reduced, and little spurious wave reflection were found in the transition zone, but the error outside of the refined region is relatively large (Düben and Korn, 2014). To further inspect whether the VR model can achieve quality simulations in the coarse regions, we conduct a comparison by adding a meridional symmetrical perturbation of the zonal wind at the southern hemisphere, as in Gassmann (2013). The initial location and magnitude of perturbation are consistent with that in the north. The values of the simulated relative vorticity in the southern hemisphere have been finally substituted by their opposite numbers to facilitate examining the differences over two hemispheres. Figure 7 shows the relative vorticity field at day 10. The QU model (Fig. 7a) produces very similar wave train in each hemisphere, although the mesh is not symmetric across the equator. In the two VR simulations (G6X4 and G5B3X4; Figs. 7b, 7c), the model resolves finer scale structures of the northern vortices. In the southern hemisphere, the pattern in G6X4 is similar to G6, though the intensity of the vortices is weaker due to its coarser resolutions. The G5B3X4 model reproduces an equivalent structure and magnitude as G6. The consistence between the VR and the QU solutions validates the reliability of the VR model for global simulations.

3.2 Multi-region refinement

The density function used above has the advantage of alleviating additional damage caused by the transition zone due to its gradual refinement. However, this formulation is restricted to a single-refinement region, which has limitation if multiple regions of interest demand higher resolutions. Enlarging the single-refinement region to cover the multiple interested areas can lead to high costs, especially when the areas are far from each other. Two multi-region refinement modes are thus examined to obtain desired resolutions in multiple regions while fix the number of the total grid points.

The first one is the hierarchical refinement mode with one refinement center. This mode contains three consecutive uniform sub-regions outside the refinement center: the 1st-refinement region, the 2nd-refinement region and the coarse-resolution region. The 2nd-refinement region provides an intermediate resolution between the 1st-refinement and coarse-resolution regions. To examine the model performance in the higher resolution simulations, we conduct the symmetrical perturbation baroclinic wave test using G8X4 superposed by the hierarchical refinement mode XL2 (i.e., G8X4L2). The refinement center is identical to the single-region refinement in Sect. 3.1. At day 10, the vortices in the southern hemisphere move into the 2nd-refinement regions (Fig. 8a). The fine-scale structures of these waves can be well simulated by the model, though the mesh resolution there is actually coarser than that in the north. To the east of the 1st-refinement region, the vorticity in the inner transition zone is also well preserved.

The hierarchical refinement mode is potentially useful to regional high-resolution modeling. However, some influencing systems far away from the refinement center may require equivalent or even finer resolution for accurate representation. Here, we adopt the second multi-region mode, the polycentric refinement mode with diverse refinement centers. We conduct the symmetrically perturbed baroclinic wave test based on a polycentric-refinement G7X4 mesh with two different refinement centers at [180° E, 35° N] and [180° E, 35° S], respectively. At day 10, the model well simulates the fine-scale structures over two refined regions (Fig. 8b). The vorticity pattern in the southern hemisphere well coincides with that in the north. Since the refinement mode is modified based on the gradual refinement type, the transition between the fine and coarse regions are smooth and stable. This refinement mode may provide an effective way to simultaneously improve the simulations at different regions.

4 Moist-atmosphere simulations

We use the idealized tropical cyclone test case (Reed and Jablonowski, 2011, 2012) as a prototype for moist-atmosphere modeling, which includes the nonlinear interaction of dynamics, moisture transport and parameterization. This test is useful to examine the VR performance because the solution does not fully converge even at 10 km resolution (e.g., Zhang et al., 2020). The simulated tropical cyclone is very sensitive to the mesh size, and higher-resolution will produce more intense storms. Two groups of numerical tests have been conducted: one group based on the nonhydrostatic solver with the DTP splitting function enabled; and one based on the hydrostatic solver with no DTP splitting (i.e., dycore, tracer transport and physics use the same time step). Most experimental configurations follow those in Zhang et al. (2020) except the time step. Results from these two groups are overall consistent. In the following main text, only the results from the nonhydrostatic model will be shown, and the results from the hydrostatic model are given in the supplement file (Figs. S2-5) for a reference.

We investigate the maintenance of the tropical cyclone when it goes across the transition zone in the hierarchical refinement mode. Given the size-controllable formulation of the density function, we evaluate two ways to examine the evolution of the tropical cyclone. The first case is to have more rapid resolution changes in the inner transition zone based on the two parameters, α_1 and λ. α_1 controls the width of the inner transition zone, and λ represents the densifying ratio between the 1st- and 2nd-refinement regions. Either narrowing the width of the transition zone or enlarging the inner densifying ratio generates a more abrupt transition zone. The other case is to have the transition zone affect the tropical cyclone in an earlier stage. The initial cyclone is placed closer to or even partly within the transition zone by increasing β_1, a parameter that denotes the coverage radius of the 1st-refinement region. In the following experiments, we use $\alpha_1 = \pi/36$, $\lambda = (1/2)^4$, and $\beta_1 = \pi/12$ to generate a G6X4L2 mesh as a reference. The 1st-refinement region in this VR mesh is ~40 km resolution. All these meshes are generated with fixed $\alpha_2 = \pi/36$ and $\beta_2 = \pi/4$.

The tropical cyclone well preserves its shape at day 10, although the transition zone possesses rapid resolution changes (Fig. 9a). The tropical cyclone is initialized at [180° E, 10° N] in the 2nd-refinement region, near the transition zone between the 1st-refinement and the 2nd-refinement regions. During its movement from the 2nd-refinement into the 1st-refinement region, the change in the grid size leads to little distortion on the tropical cyclone in each experiment. The wind speed distributions of the tropical cyclone across the abrupt transition zone in several tests using different meshes (Figs. 9b-9d) are quite close to that in Fig. 9a. In the control run, a minor cyclonic disturbance appears in the 2nd-refinement region. When the inner transition zone becomes narrower, this disturbance gets stronger due to the larger area of this QU region. The location of the minor cyclonic disturbance is affected by the mesh distribution around the transition zone. In contrast, the major cyclone maintains its strength and shape regardless of the mesh variation.

To verify this result, we examine the model sensitivity by conducting a series of experiments based on the three parameters (Fig. 10). Only one of the three parameters is altered for each experiment, as shown in the legends. The minimum surface pressure (Figs. 10a-10c) and maximum wind speed at 850 hPa (Figs. 10d-10f) are used as two proxies to quantify the intensity of the tropical cyclone. The tropical cyclone rapidly strengthens in the first two days before it turns into a gently developing stage in each experiment. The evolution of the intensity is diverse when each of the three parameters changes. However, the final intensity of the cyclone in the experiments is overall comparable, suggesting that the VR solutions are consistent.

https://doi.org/10.5194/gmd-2020-150
Preprint. Discussion started: 7 July 2020

Geoscientific Model Development Discussions

Ringler et al. (2011) suggested that the global solution error is controlled primarily by the coarsest-resolution region in a shallow-water VR model. Our tests imply that for the VR model, the simulation quality of the fine-scale fluid structures is largely determined by the finest resolution, and other configurations only have a minor role in this regard. It should be also noted that the tropical clone is overall stronger in each VR simulation than in the QU case that has the same number of points. The tropical cyclone is initialized in the 2nd-refinement region of the VR mesh. The rapid deepening of tropical cyclone in its early development stage benefits from the higher resolution of the 2nd-refinement region than the QU mesh. The cyclone still develops faster than the uniform one when it moves across the inner transition zone.

To further investigate the fine-scale resolving ability of the VR model under higher resolution, we conduct this test case based on the G7X4L2 mesh. The mesh parameters are as same as G6X4L2. The 1st-refinement region in the G7X4L2 mesh is at ~20 km resolution. Fig. 11 shows the horizontal (850 hPa; Figs. 11a-11d) and vertical distribution (Figs. 11e-11h) of the horizontal wind speed in QU and VR simulations. The tropical cyclone strengthens after it moves through the transition zone of the G6X4L2 mesh. Compared to the QU-mesh model, the wind speed distribution is more symmetric in the VR model. The maximum wind band of the cyclone converges towards its center, almost within 1 degree from the center. Moving to G7, the VR model based on the G7X4L2 mesh produces stronger storms. The meridional distribution of its wind speed is nearly symmetric. The tropical cyclone expands to higher vertical levels and its intensity increases. The VR model well captures the intensity and structure of the tropical cyclone in its higher-resolution region. The hydrostatic model (Fig. S4) are overall consistent with the nonhydrostatic model, with a slightly stronger tropical cyclone.

Previous studies have shown that in the QU-mesh models, the tropical cyclone reduces its area coverage while strengthens its intensity as the resolution increases (e.g., Fig. 3 in Zarzycki et al., 2014; Zhang et al., 2020). Our results present a similar feature that the tropical cyclone possesses a smaller area coverage and higher intensity in the refined regions, as compared to the QU model that has the same number of grid points. Moreover, we have found that the intensity of the tropical cyclone is also influenced by the Smagorinsky horizontal diffusion coefficient (Fig. 12). For the QU G6 mesh (Figs. 12a, 12b), as the coefficient becomes smaller, the minimum surface pressure decreases and the maximum wind speed at 850 hPa increases. Although G6X4L2 shows similar variations as the coefficient decreases (Figs. 12e, 12f), it exhibits higher sensitivity to the coefficient. Such difference still exists when the grid points increases up to G7 (Figs. 12c, 12d, 12g, 12h). This highlights that for a VR model, a proper model configuration with well-tuned parameters is more important to achieve good performance.

5 Conclusions

In this study, a global unstructured-mesh model is systematically tested and evaluated based on its VR configuration. We propose various refinement approaches and evaluate the model behaviors with the aid of dry and moist idealized test cases. The major conclusion is summarized as follows.

(i) Regarding the single-region refinement mode, the VR model possesses comparable accuracy compared to the QU one. The G5B3X4 VR-mesh, which has about half number of grid points in the QU mesh G7, can capture the fine-scale structure of vorticity in the fine-resolution region, closer to G8 than G7. In the transition zone, the vorticity is not adversely affected by the variation of the mesh resolution. In the coarse region, G5B3X4 reproduces an equivalent distribution of vorticity as the lower-resolution G6. The multi-region refinement modes provide a more flexible way to achieve desired resolution of multiple regions of interest. In these modes, the model also simulates the general pattern well, with the ability to resolve fine-scale filament structures of the vortices.

(ii) For moist-atmosphere modeling, the VR model exhibits stability and robustness. In the hierarchical refinement mode, a series of sensitivity tests based on the three refinement parameters validates the maintenance of the tropical cyclone across the transition zone under the diverse refinement environment. The simulation of the fine-scale structure is mainly controlled by the finest-resolution region. The tropical cyclone rapidly develops in the vicinity of the inner mesh transition zone. Compared to the QU model with the same number of grid points, the VR model simulates a stronger cyclone, with its maximum wind band converging towards the cyclone center. Such a variation is similar to resolution sensitivity supported by the QU-mesh models. The difference between the VR and QU models lies in their sensitivity to the Smagorinsky horizontal diffusion coefficient: a higher coefficient tends to weaken the storm, and the VR model exhibits higher sensitivity than the QU-mesh model in this regard.

Code and data availability: GRIST is available at https://github.com/grist-dev, in private repositories. A way is provided for the editor and reviewers to access the code, which does not compromise their anonymity (to our best effort). A version of the model code, running and postprocessing scripts for supporting this paper are available at: https://zenodo.org/record/3930643. The grid data used to enable the tests are located at https://zenodo.org/record/3817060. The entire model code is in an active development stage subject to several projects. Full access is available to a member or a collaborator. The authority request may be sent to grist_dev@163.com.

Supplement: vr_supplement.pdf contains Table S1, S2; Figs. S1-S5.

Author contribution: Y. Zhou performed mesh generation, numerical experiments, data analysis, with inputs from Y. Zhang, and wrote the initial manuscript. Y. Zhang developed the model, designed this study and revised the manuscript. J. Li supervised the project of model development. R. Yu supervised the team member and provided impetus and resources. Z. Liu is responsible for parallel computing, and customized the parallel mesh generation software for GRIST. All the authors continuously discussed the model development and the results of the manuscript.

Competing interests. The authors declare that they have no conflict of interest.

Acknowledgments. This study was supported by the National Natural Science Foundation of China (41875135), the National Key R&D Program of China (2017YFC1502202, 2016YFA0602101), and the S&T Development Fund of CAMS (2019KJ011).

References

Bacmeister, J. T., Wehner, M. F., Neale, R. B., Gettelman, A., Hannay, C., Lauritzen, P. H., Caron, J. M., and Truesdale, J. E.: Exploratory High-Resolution Climate Simulations using the Community Atmosphere Model (CAM), J. Climate, 27, 3073-3099, doi:10.1175/jcli-d-13-00387.1, 2014.

Du, Q., Faber, V., and Gunzburger, M.: Centroidal Voronoi tessellations: Applications and algorithms, Siam Rev, 41, 637-676, 1999.

Düben, P. D. and Korn, P.: Atmosphere and Ocean Modeling on Grids of Variable Resolution—A 2D Case Study, Mon. Wea. Rev., 142, 1997-2017, doi:10.1175/mwr-d-13-00217.1, 2014.

Gassmann, A.: A global hexagonal C-grid non-hydrostatic dynamical core (ICON-IAP) designed for energetic consistency, Quart. J. Roy. Meteor. Soc., 139, 152-175, doi:10.1002/qj.1960, 2013.

Gettelman, A., Callaghan, P., Larson, V. E., Zarzycki, C. M., Bacmeister, J. T., Lauritzen, P. H., Bogenschutz, P. A., and Neale, R. B.: Regional Climate Simulations With the Community Earth System Model, J Adv Model Earth Sy, 10, 1245-1265, doi:10.1002/2017ms001227, 2018.

Guba, O., Taylor, M. A., Ullrich, P. A., Overfelt, J. R., and Levy, M. N.: The spectral element method (SEM) on variable-resolution grids: evaluating grid sensitivity and resolution-aware numerical viscosity, Geosci. Model Dev., 7, 2803-2816, doi:10.5194/gmd-7-2803-2014, 2014.

Harris, L. M., Lin, S.-J., and Tu, C.: High-Resolution Climate Simulations Using GFDL HiRAM with a Stretched Global Grid, J. Climate, 29, 4293-4314, doi:10.1175/jcli-d-15-0389.1, 2016.

Hashimoto, A., Done, J. M., Fowler, L. D., and Bruyère, C. L.: Tropical cyclone activity in nested regional and global grid-refined simulations, Climate Dyn., 47, 497-508, doi:10.1007/s00382-015-2852-2, 2015.

Hendricks, E. A., Kopera, M. A., Giraldo, F. X., Peng, M. S., Doyle, J. D., and Jiang, Q.: Evaluation of the Utility of Static and Adaptive Mesh Refinement for Idealized Tropical Cyclone Problems in a Spectral Element Shallow-Water Model, Mon. Wea. Rev., 144, 3697-3724, doi:10.1175/mwr-d-15-0146.1, 2016.

Huang, X., Rhoades, A. M., Ullrich, P. A., and Zarzycki, C. M.: An evaluation of the variable‐resolution CESM for modeling California's climate, J Adv Model Earth Sy, 8, 345-369, doi:10.1002/2015ms000559, 2016.

Jablonowski, C. and Williamson, D. L.: A baroclinic instability test case for atmospheric model dynamical cores, Quart. J. Roy. Meteor. Soc., 132, 2943-2975, doi:10.1256/qj.06.12, 2006.

Jacobsen, D. W., Gunzburger, M., Ringler, T., Burkardt, J., and Peterson, J.: Parallel algorithms for planar and spherical Delaunay construction with an application to centroidal Voronoi tessellations, Geosci. Model Dev., 6, 1353-1365, doi:10.5194/gmd-6-1353-2013, 2013.

Ju, L.: Conforming centroidal Voronoi Delaunay triangulation for quality mesh generation, Int J Numer Anal Mod, 4, 531-547, 2007.

Ju, L., Ringler, T., and Gunzburger, M.: Voronoi Tessellations and Their Application to Climate and Global Modeling, in: Numerical Techniques for Global Atmospheric Models, edited by: Lauritzen, P., Jablonowski, C., Taylor, M., and Nair, R., Lecture Notes in Computational Science and Engineering, Springer Berlin Heidelberg, Berlin, Heidelberg, 313-342, 2011.

Jung, T., Miller, M. J., Palmer, T. N., Towers, P., Wedi, N., Achuthavarier, D., Adams, J. M., Altshuler, E. L., Cash, B. A., Kinter, J. L., Marx, L., Stan, C., and Hodges, K. I.: High-Resolution Global Climate Simulations with the ECMWF Model in Project Athena: Experimental Design, Model Climate, and Seasonal Forecast Skill, J. Climate, 25, 3155-3172, doi:10.1175/jcli-d-11-00265.1, 2012.

Liu, Y. and Yang, T.: Impact of Local Grid Refinements of Spherical Centroidal Voronoi Tessellations for Global Atmospheric Models, Commun Comput Phys, 21, 1310-1324, doi:10.4208/cicp.050815.020916a, 2017.

Metropolis, N. and Ulam, S.: The Monte Carlo Method, J. Am. Stat. Assoc., 44, 335-341, doi:10.1080/01621459.1949.10483310, 1949.

Park, S.-H., Skamarock, W. C., Klemp, J. B., Fowler, L. D., and Duda, M. G.: Evaluation of Global Atmospheric Solvers Using Extensions of the Jablonowski and Williamson Baroclinic Wave Test Case, Mon. Wea. Rev., 141, 3116-3129, doi:10.1175/mwr-d-12-00096.1, 2013.

Rauscher, S. A., Ringler, T. D., Skamarock, W. C., and Mirin, A. A.: Exploring a Global Multiresolution Modeling Approach Using Aquaplanet Simulations, J. Climate, 26, 2432-2452, doi:10.1175/jcli-d-12-00154.1, 2013.

Rauscher, S. A. and Ringler, T. D.: Impact of Variable-Resolution Meshes on Midlatitude Baroclinic Eddies Using CAM-MPAS-A, Mon. Wea. Rev., 142, 4256-4268, doi:10.1175/mwr-d-13-00366.1, 2014.

Reed, K. A. and Jablonowski, C.: An Analytic Vortex Initialization Technique for Idealized Tropical Cyclone Studies in AGCMs, Mon. Wea. Rev., 139, 689-710, doi:10.1175/2010mwr3488.1, 2011.

Reed, K. A. and Jablonowski, C.: Idealized tropical cyclone simulations of intermediate complexity: A test case for AGCMs, J Adv Model Earth Sy, 4, n/a-n/a, doi:10.1029/2011ms000099, 2012.

Ringler, T., Ju, L., and Gunzburger, M.: A multiresolution method for climate system modeling: application of spherical centroidal Voronoi tessellations, Ocean Dynamics, 58, 475-498, doi:10.1007/s10236-008-0157-2, 2008.

Ringler, T. D., Jacobsen, D., Gunzburger, M., Ju, L., Duda, M., and Skamarock, W.: Exploring a Multiresolution Modeling Approach within the Shallow-Water Equations, Mon. Wea. Rev., 139, 3348-3368, doi:10.1175/mwr-d-10-05049.1, 2011.

Sabin, T. P., Krishnan, R., Ghattas, J., Denvil, S., Dufresne, J. L., Hourdin, F., and Pascal, T.: High resolution simulation of the South Asian monsoon using a variable resolution global climate model, Climate Dyn., 41, 173-194, doi:10.1007/s00382-012-1658-8, 2013.

Sakaguchi, K., Leung, L. R., Zhao, C., Yang, Q., Lu, J., Hagos, S., Rauscher, S. A., Dong, L., Ringler, T. D., and Lauritzen, P. H.: Exploring a Multiresolution Approach Using AMIP Simulations, J. Climate, 28, 5549-5574, doi:10.1175/jcli-d-14-00729.1, 2015.

Smagorinsky, J.: General Circulation Experiments with the Primitive Equations, Mon. Wea. Rev., 91, 99-164, doi:10.1175/1520-0493(1963)091<0099:Gcewtp>2.3.Co;2, 1963.

St-Cyr, A., Jablonowski, C., Dennis, J. M., Tufo, H. M., and Thomas, S. J.: A Comparison of Two Shallow-Water Models with Nonconforming Adaptive Grids, Mon. Wea. Rev., 136, 1898-1922, doi:10.1175/2007mwr2108.1, 2008.

Strachan, J., Vidale, P. L., Hodges, K., Roberts, M., and Demory, M.-E.: Investigating Global Tropical Cyclone Activity with a Hierarchy of AGCMs: The Role of Model Resolution, J. Climate, 26, 133-152, doi:10.1175/jcli-d-12-00012.1, 2013.

Walsh, K., Lavender, S., Scoccimarro, E., and Murakami, H.: Resolution dependence of tropical cyclone formation in CMIP3 and finer resolution models, Climate Dyn., 40, 585-599, doi:10.1007/s00382-012-1298-z, 2012.

Wang, L., Zhang, Y., Li, J., Liu, Z., and Zhou, Y.: Understanding the Performance of an Unstructured-Mesh Global Shallow Water Model on Kinetic Energy Spectra and Nonlinear Vorticity Dynamics, J. Meteor. Res., 33, 1075-1097, doi:10.1007/s13351-019-9004-2, 2019.

Wehner, M. F., Reed, K. A., Li, F., Prabhat, Bacmeister, J., Chen, C.-T., Paciorek, C., Gleckler, P. J., Sperber, K. R., Collins, W. D., Gettelman, A., and Jablonowski, C.: The effect of horizontal resolution on simulation quality in the Community Atmospheric Model, CAM5.1, J Adv Model Earth Sy, 6, 980-997, doi:10.1002/2013ms000276, 2014.

Weller, H., Weller, H. G., and Fournier, A.: Voronoi, Delaunay, and Block-Structured Mesh Refinement for Solution of the Shallow-Water Equations on the Sphere, Mon. Wea. Rev., 137, 4208-4224, doi:10.1175/2009mwr2917.1, 2009.

Wicker, L. J. and Skamarock, W. C.: Time-Splitting Methods for Elastic Models Using Forward Time Schemes, Mon. Wea. Rev., 130, 2088-2097, doi:10.1175/1520-0493(2002)130<2088:Tsmfem>2.0.Co;2, 2002.

Yu, R.: A two-step shape-preserving advection scheme, Adv. Atmos. Sci., 11, 479-490, doi:10.1007/BF02658169, 1994.

https://doi.org/10.5194/gmd-2020-150
Preprint. Discussion started: 7 July 2020

Geoscientific Model Development Discussions
Open Access
EGU

Yu, R., Zhang, Y., Wang, J., Li, J., Chen, H., Gong, J., and Chen, J.: Recent Progress in Numerical Atmospheric Modeling in China, Adv. Atmos. Sci., 36, 938-960, doi:10.1007/s00376-019-8203-1, 2019.

Zarzycki, C. M. and Jablonowski, C.: A multidecadal simulation of Atlantic tropical cyclones using a variable-resolution global atmospheric general circulation model, J Adv Model Earth Sy, 6, 805-828, doi:10.1002/2014ms000352, 2014.

Zarzycki, C. M., Jablonowski, C., and Taylor, M. A.: Using Variable-Resolution Meshes to Model Tropical Cyclones in the Community Atmosphere Model, Mon. Wea. Rev., 142, 1221-1239, doi:10.1175/mwr-d-13-00179.1, 2014.

Zhang, Y., Chen, H., and Yu, R.: Simulations of Stratus Clouds over Eastern China in CAM5: Sensitivity to Horizontal Resolution, J. Climate, 27, 7033-7052, doi:10.1175/jcli-d-13-00732.1, 2014.

Zhang, Y., Yu, R., and Li, J.: Implementation of a conservative two-step shape-preserving advection scheme on a spherical icosahedral hexagonal geodesic grid, Adv. Atmos. Sci., 34, 411-427, doi:10.1007/s00376-016-6097-8, 2017.

Zhang, Y.: Extending High-Order Flux Operators on Spherical Icosahedral Grids and Their Applications in the Framework of a Shallow Water Model, J Adv Model Earth Sy, 10, 145-164, doi:10.1002/2017ms001088, 2018.

Zhang, Y., Li, J., Yu, R., Zhang, S., Liu, Z., Huang, J., and Zhou, Y.: A Layer ‐ Averaged Nonhydrostatic Dynamical Framework on an Unstructured Mesh for Global and Regional Atmospheric Modeling: Model Description, Baseline Evaluation, and Sensitivity Exploration, J Adv Model Earth Sy, 11, 1685-1714, doi:10.1029/2018ms001539, 2019.

Zhang, Y., Li, J., Yu, R., Liu, Z., Zhou, Y., Li, X., and Huang, X.: A Multiscale Dynamical Model in a Dry-mass Coordinate for Weather and Climate Modeling: Moist Dynamics and its Coupling to Physics, Mon. Wea. Rev., doi:10.1175/mwr-d-19-0305.1, 2020.

https://doi.org/10.5194/gmd-2020-150
Preprint. Discussion started: 7 July 2020

Geoscientific Model Development Discussions
Open Access

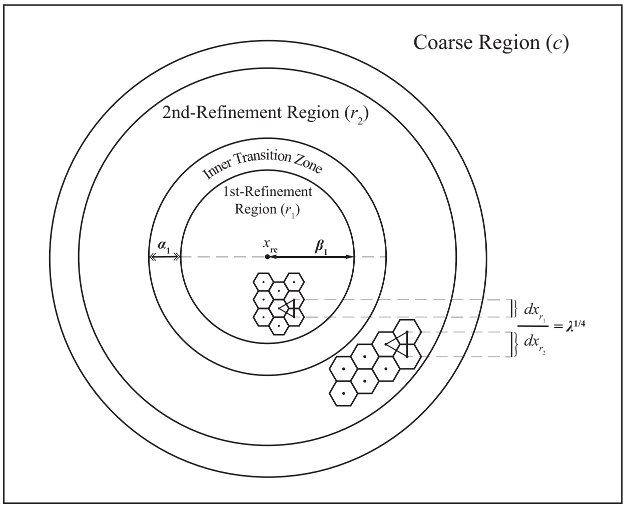

Figure 1: A schematic diagram of the hierarchical refinement mesh, illustrating the function of three parameters of the density function. α_1 controls the width of the inner transition zone; λ represents the inner densifying ratio between the 1st-refinement and 2nd-refinement resolution regions; β_1 denotes the coverage radius of the 1st-refinement region.

https://doi.org/10.5194/gmd-2020-150
Preprint. Discussion started: 7 July 2020

Geoscientific Model Development Discussions
Open Access

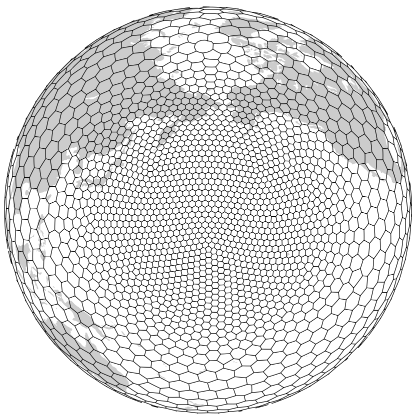

Figure 2: An illustration of the X4 variable-resolution mesh used for the baroclinic wave test with the refinement center x_{rc} at [180° E, 35° N], $\alpha = \pi/20$, and $\beta = \pi/6$. The mesh sizes are scaled up here for a clear vision of each grid cell based on reduced generators.

https://doi.org/10.5194/gmd-2020-150
Preprint. Discussion started: 7 July 2020

Geoscientific Model Development Discussions
Open Access
EGU

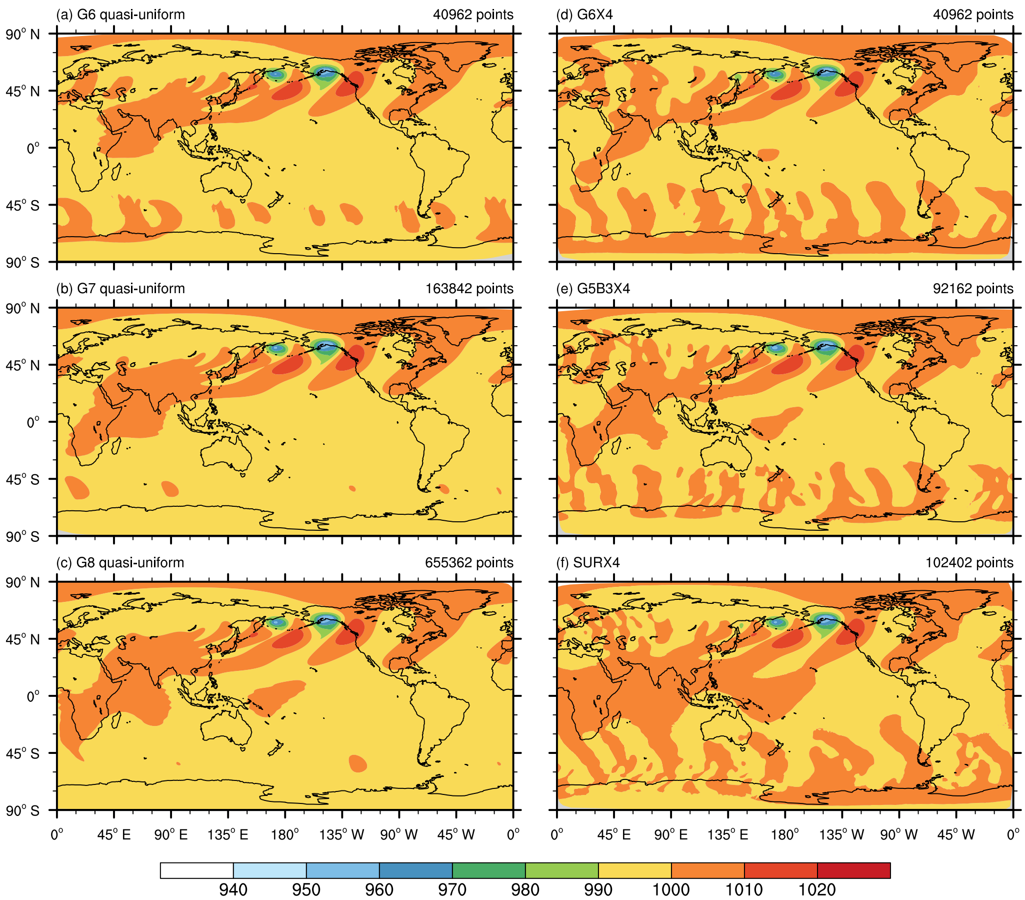

Figure 3: Baroclinic wave test: surface pressure (unit: hPa) at day 9 simulated by the nonhydrostatic model with (a-c) quasi-uniform and (d-f) variable-resolution meshes.

https://doi.org/10.5194/gmd-2020-150
Preprint. Discussion started: 7 July 2020

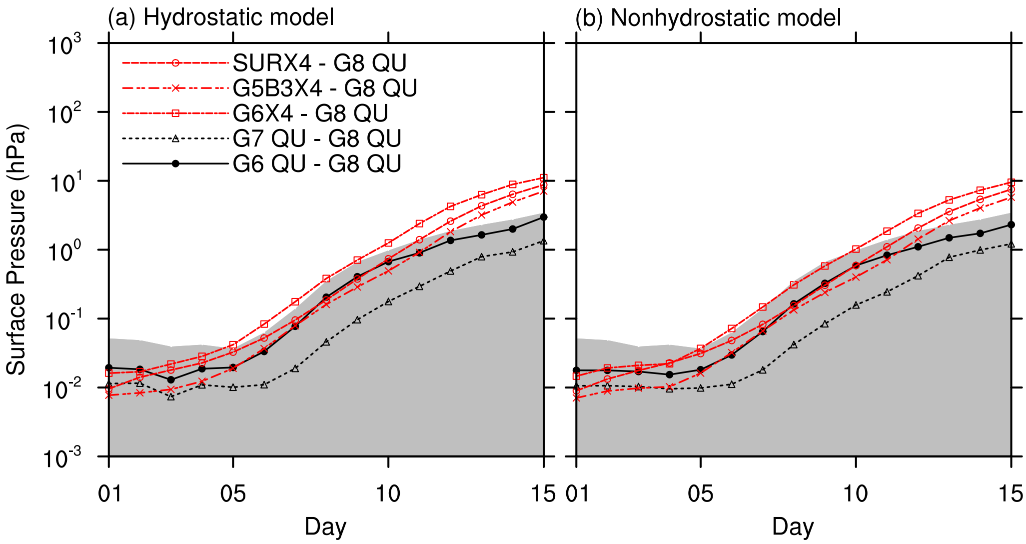

Figure 4: Baroclinic wave test: the l_2 error norms of surface pressure as a function of time for (a) the hydrostatic and (b) the nonhydrostatic dynamical core. The error of the low-resolution quasi-uniform mesh (black) and the variable-resolution mesh (red) is computed against the high-resolution quasi-uniform G8 mesh. The gray area denotes the uncertainty in the reference solutions, which selects the maximum l_2 error norms from four curves (the quasi-uniform G7 and G8 cases considering the hydrostatic and nonhydrostatic dynamical core as two models), following Jablonowski and Williamson (2006).

https://doi.org/10.5194/gmd-2020-150
Preprint. Discussion started: 7 July 2020

Geoscientific Model Development Discussions

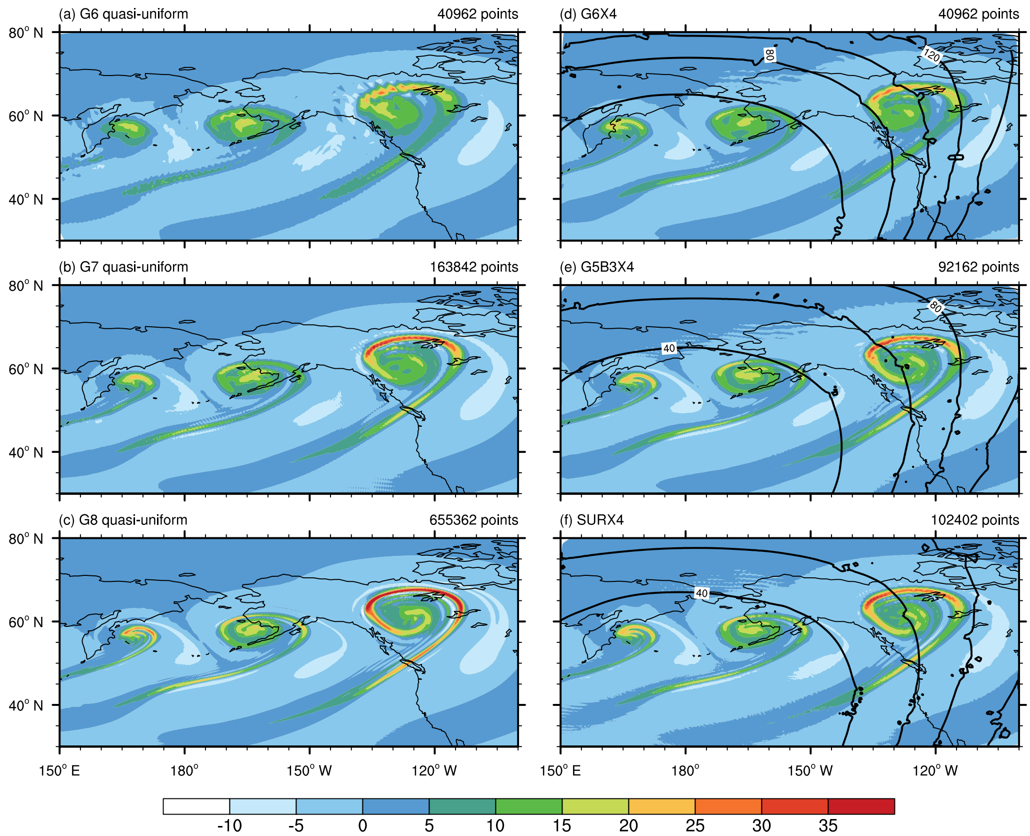

Figure 5: As in Fig. 3, but for relative vorticity (10^{-5} s^{-1}) at the model level near 850 hPa after 10 simulation days. The contour lines denote the mesh resolutions (in kilometer). The vorticity is defined and displayed on the raw triangular grid (also true for Figs. 7 and 8). See Fig. S1 for the remapped QU-mesh solutions on the regular latitude longitude grid.

https://doi.org/10.5194/gmd-2020-150
Preprint. Discussion started: 7 July 2020

Geoscientific Model Development
Discussions

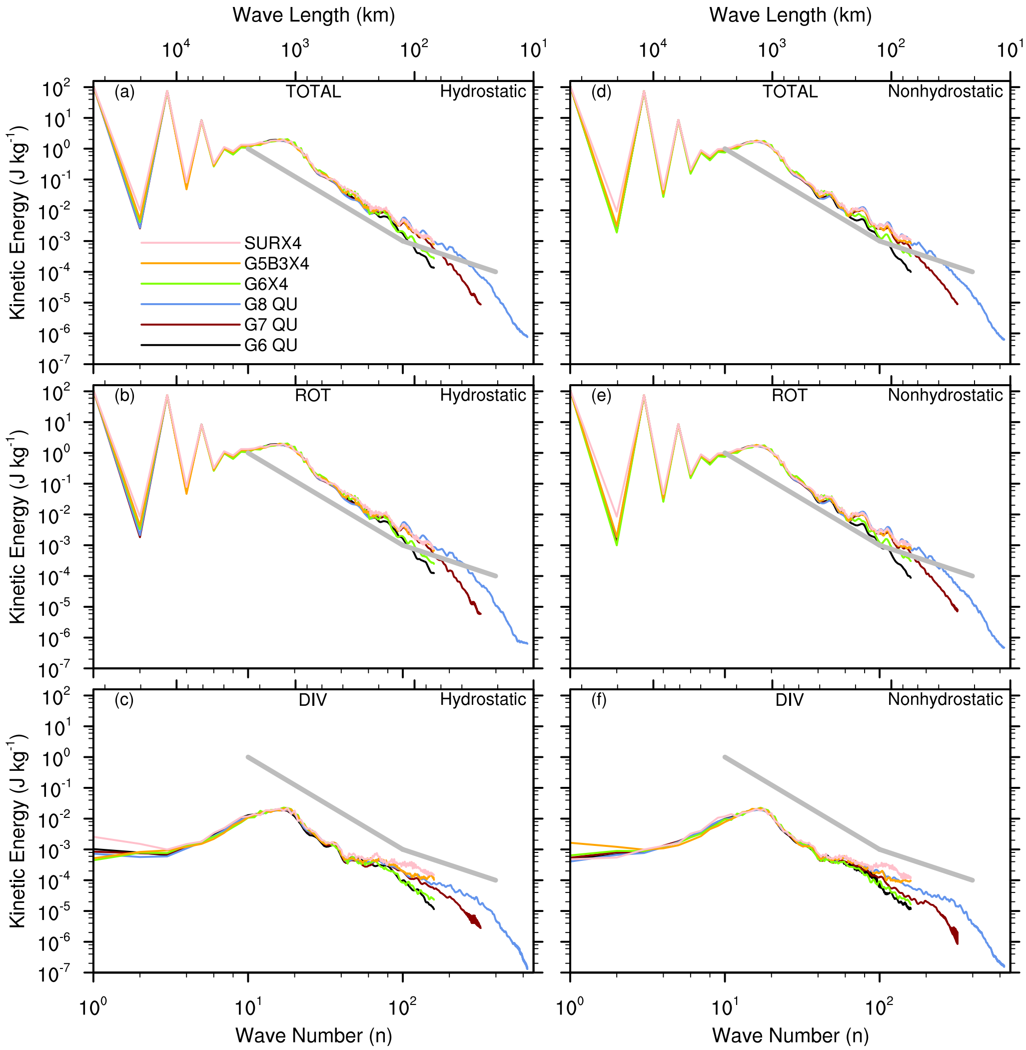

Figure 6: Baroclinic wave test: horizontal kinetic energy spectra at the model level near 850 hPa at day 10 in terms of (a) the total kinetic energy, (b) the rotational component, and (c) the divergence component, based on quasi-uniform and variable-resolution meshes. Results from the hydrostatic (left column) and nonhydrostatic (right column) dynamical core are shown. The thick gray lines denote the −3 and −5/3 slopes, respectively. Units: J kg^{-1}.

https://doi.org/10.5194/gmd-2020-150
Preprint. Discussion started: 7 July 2020

Geoscientific Model Development
Discussions
Open Access

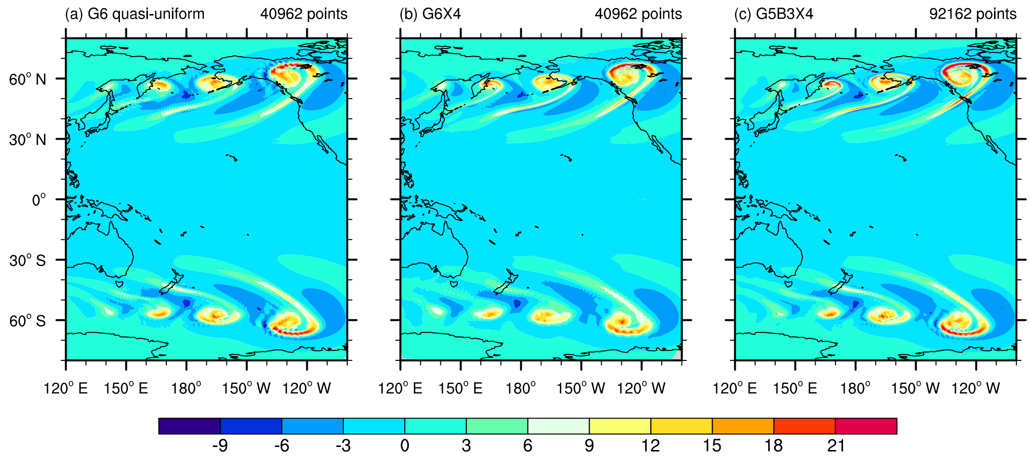

Figure 7: Adding a symmetrical perturbation in the southern hemisphere for the baroclinic wave test: relative vorticity (10^{-5} s^{-1}) at the model level near 850 hPa at day 10 simulated by the dry dynamical core with (a) quasi-uniform G6, (b) variable-resolution G6X4, and (c) G5B3X4 meshes. The values in the southern hemisphere are substituted by their opposite numbers for a clear comparison. Data are displayed on the raw triangular grid that defines vorticity.

https://doi.org/10.5194/gmd-2020-150
Preprint. Discussion started: 7 July 2020

Geoscientific Model Development Discussions
Open Access

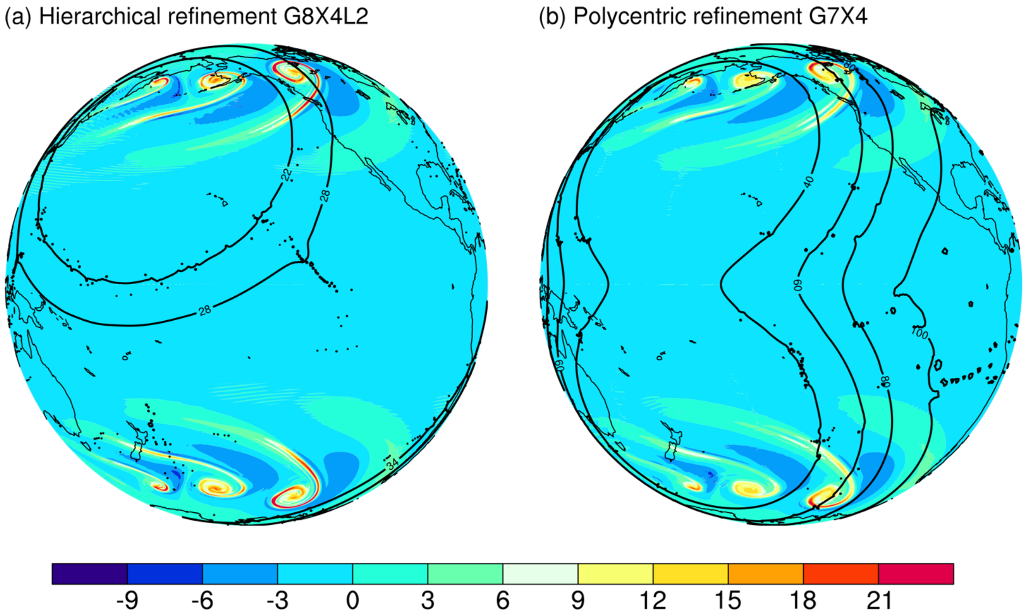

Figure 8: As in Fig. 7, but for the two multi-region refinement meshes: (a) the hierarchical refinement mesh G8X4L2 and (b) the polycentric refinement mesh based on G7X4. The contour lines denote the mesh resolutions (km).

https://doi.org/10.5194/gmd-2020-150
Preprint. Discussion started: 7 July 2020

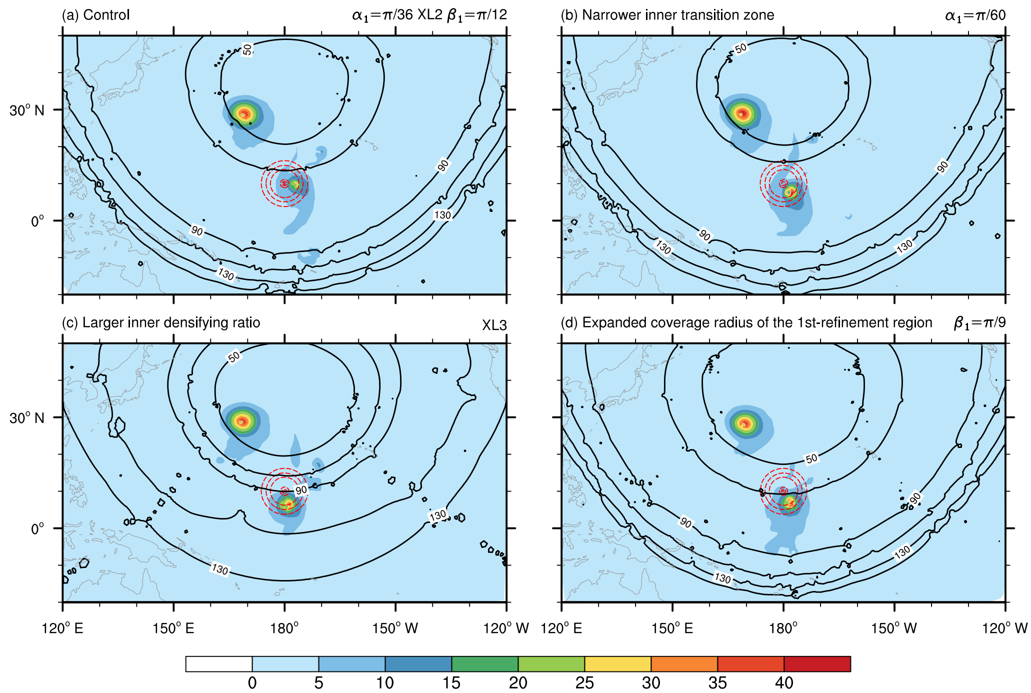

Figure 9: Idealized tropical cyclone test: the horizontal wind speed (m s^{-1}) at 850 hPa after 10 simulation days based on hierarchical refinement meshes with (a) the control, (b) reduced α_1 and (c) higher λ for more rapid changes in the mesh resolution of the transition zone, and (d) larger β_1 to make the transition zone affect the tropical cyclone in an earlier stage. The red dashed lines mark the initial location of the tropical cyclone. The black contour lines denote the mesh resolutions (km).

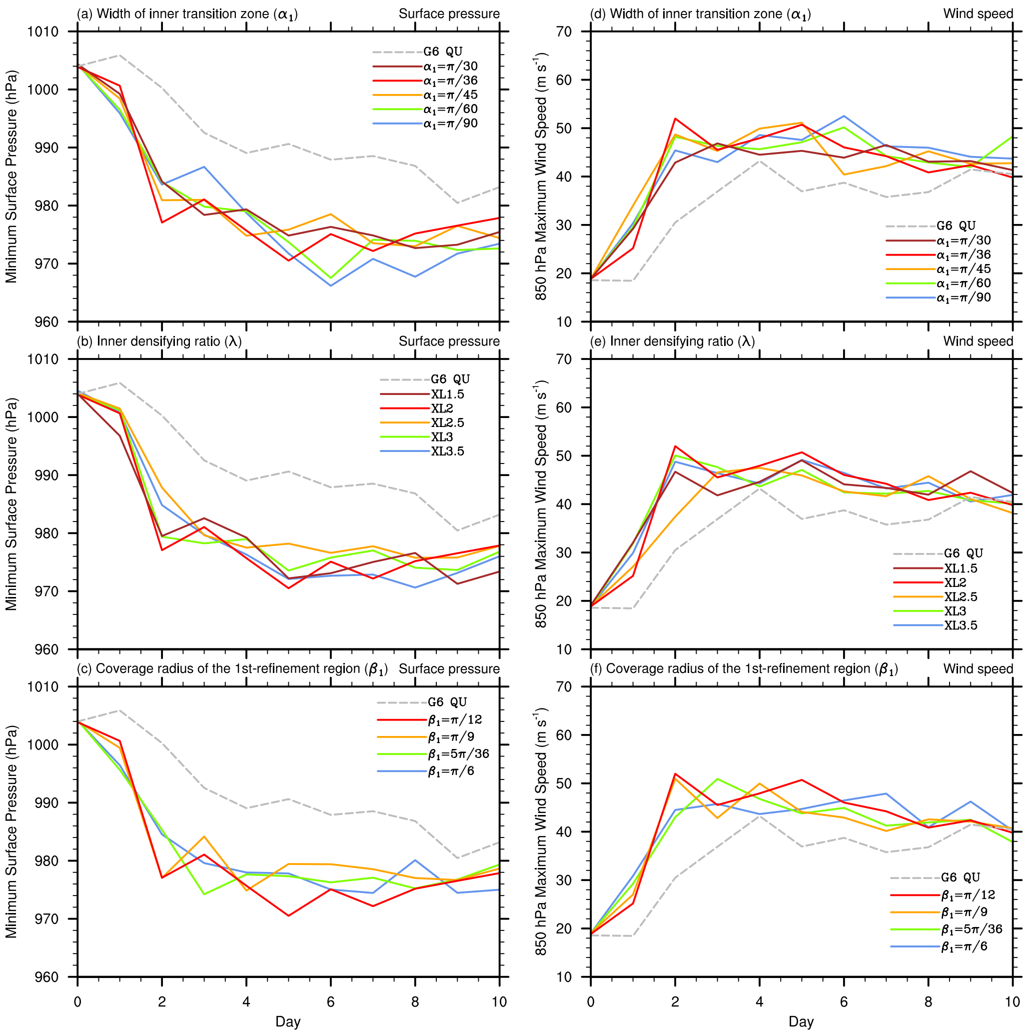

Figure 10: Idealized tropical cyclone test: temporal evolution of minimum surface pressure and maximum 850-hPa horizontal wind speed based on the quasi-uniform G6 and hierarchical refinement meshes with (a, d) α_1, (b, e) λ, and (c, f) β_1 changed in the sensitivity tests. As one parameter is changed, the other two parameters are fixed according to the control run with $\alpha_1 = \pi/36$, $\lambda = (1/2)^4$ (i.e., XL2), and $\beta_1 = \pi/12$. The three mesh parameters denote the width of the inner transition zone, the inner densifying ratio, and the coverage radius of the 1st-refinement region, respectively.

https://doi.org/10.5194/gmd-2020-150
Preprint. Discussion started: 7 July 2020

Geoscientific Model Development Discussions

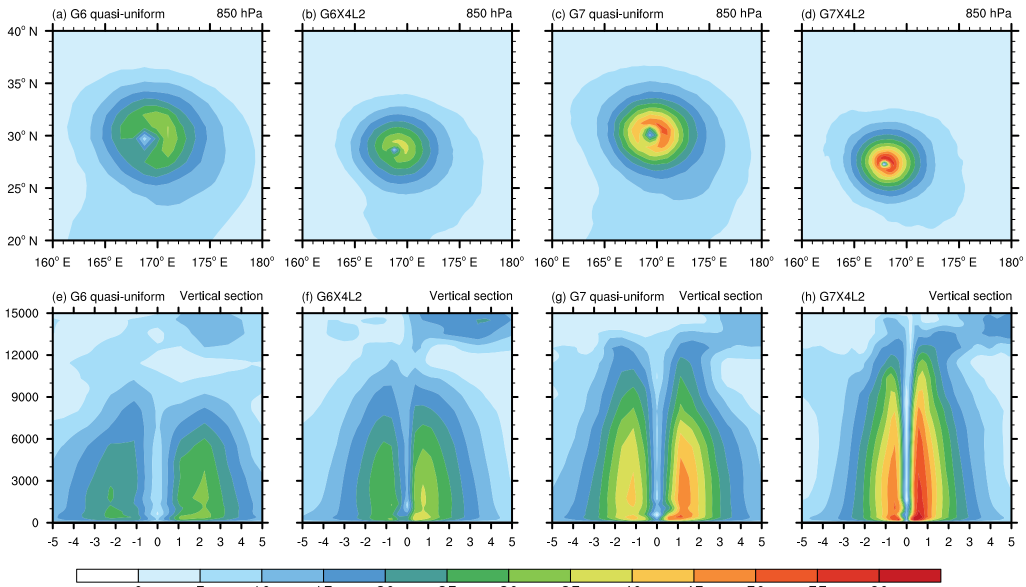

549

550 **Figure 11: Idealized tropical cyclone test: (a-d) the horizontal wind speed (m s[-1]) at 850 hPa after 10 simulation days based**
551 **on quasi-uniform and variable-resolution meshes and (e-h) the corresponding vertical cross section of the wind speed with a**
552 **meridional range of ±5-degree apart from the center of the tropical cyclone. The vertical coordinate of the cross section**
553 **denotes the height (m).**

https://doi.org/10.5194/gmd-2020-150
Preprint. Discussion started: 7 July 2020

Geoscientific Model Development
Discussions

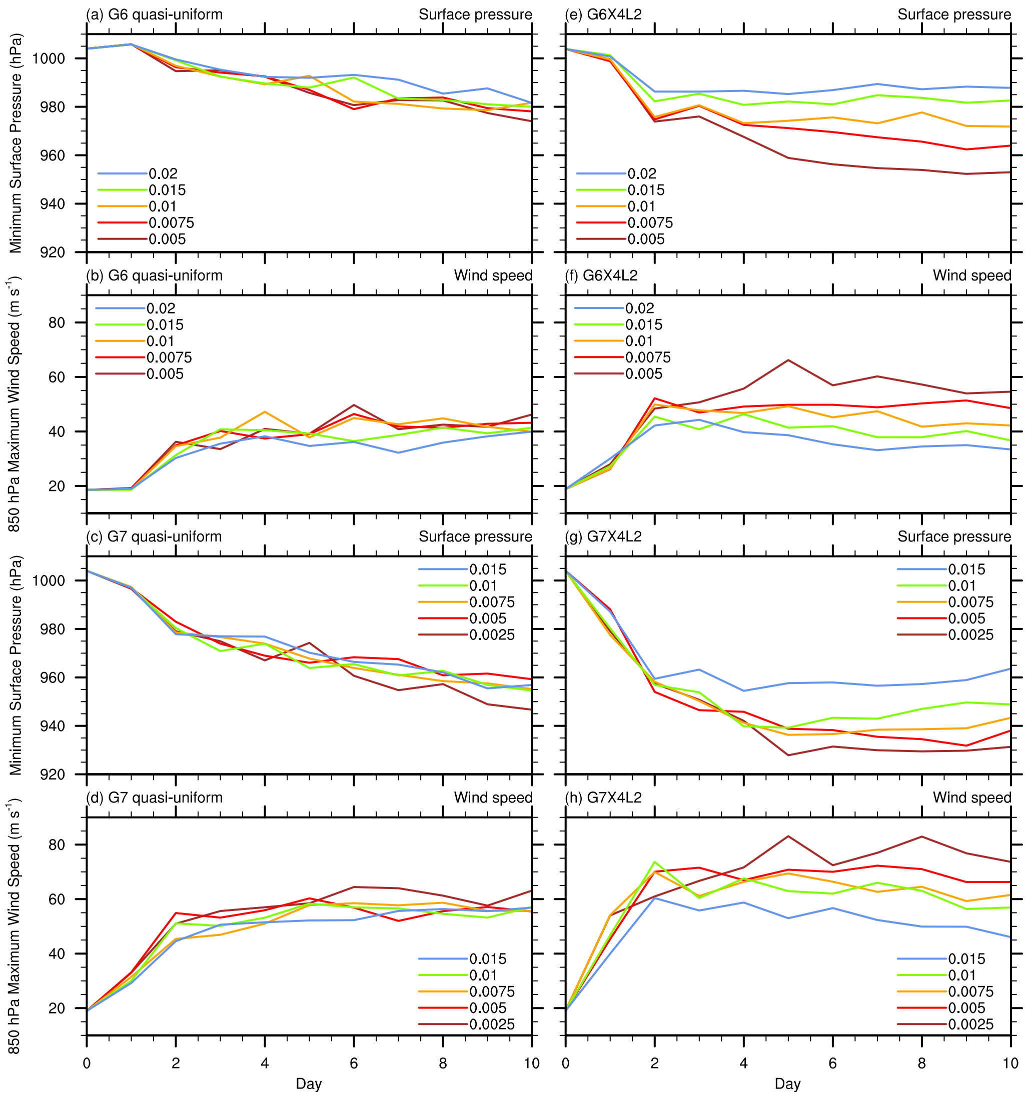

554
555 **Figure 12: Idealized tropical cyclone test: temporal evolution of minimum surface pressure and maximum 850-hPa**
556 **horizontal wind speed based on the quasi-uniform meshes (left column) and hierarchical refinement meshes (right column)**
557 **with decreasing Smagorinsky horizontal diffusion coefficients marked by colors.**